Chemical Science

ROYAL SOCIETY OF CHEMISTRY

EDGE ARTICLE

View Article Online
View Journal

Cite this: DOI: 10.1039/d6sc01073c

All publication charges for this article have been paid for by the Royal Society of Chemistry

Homoconjugation-induced enhancements of photophysical properties in donor–acceptor triptycenes arise from interplay between intramolecular charge transfer and exciton states

Stefan Warrington,[ab] Hristo Ivov Gonev,[c] Gary S. Nichol,[a] Eleanor M. Dodd,[d] Simon J. Coles,[d] Thomas J. Penfold,[e] Marc K. Etherington,[f] Tracey M. Clarke *[c] and Iain A. Wright *[a]

Received 6th February 2026
Accepted 5th June 2026

DOI: 10.1039/d6sc01073c

rsc.li/chemical-science

Strategies for tuning the optical properties of organic chromophores generally focus on shifting the edges of the spectrum: this might be red-shifting the longest absorbance band to improve solar absorbance, or blue-shifting of the highest energy emission band towards deep blue emission. In contrast, strategies to enhance molar absorptivity and control excited state rate constants are less obvious, with intermolecular excitons such as *J*-aggregates providing arguably the most powerful approach. Here, a homologous series of π-extended triptycenes is presented which reveal opportunities to control both aspects. These molecules have electronic spectra consisting of two distinct regimes, a low energy intramolecular charge transfer and a mid-spectral progression which has characteristics similar to that of a *J*-aggregate in several respects. This reveals that a homoconjugated framework can be utilised rationally to separate and independently control distinct regions of the electronic structure of the molecule, here leading to controllably amplified mid-spectrum absorbance intensities and high fluorescence quantum yields.

Introduction

Covalently-linked chromophore assemblies with three-dimensional (3D) branched topologies are a promising class of molecular materials for organic energy conversion technologies.[1] This is especially apparent in the optoelectronic properties of systems where the chromophores are held in sufficiently close proximity to facilitate interchromophore interactions.[2–9] Benefits of such architectures may include improved photoabsorbance cross-sections, thin film morphologies and interfacing which can improve performance in organic photovoltaics (OPVs)[10–16] or exert control over the excited state behaviour of emitters for organic light-emitting devices (OLEDs)[17–23] and related technologies.

The trefoil molecule triptycene has a robust 3D carbon framework from which to construct such systems by appending chromophores onto the three fins. It also provides a distinctive route to encourage electronic communication between the appended chromophores through homoconjugation.[24] Homoconjugation is the through-space orbital overlap of two π-systems separated by a single non-conjugated atom or group, in iptycenes these are the bridgehead sp^3 carbon atoms.[25,26]

In triptycene-based intramolecular charge transfer (ICT) emitters, positive influences on photophysical properties have been observed. These include very large enhancements in molar absorptivities (ε) and oscillator strengths (f_{osc}), higher photoluminescence quantum yields (Φ) and acceleration of rate constants facilitated by increased spin–orbit coupling (SOC). Observations made of results to date suggest that if large positive influences are to be observed then it is imperative that the lowest unoccupied molecular orbital (LUMO) be localised over the homoconjugated iptycene core.[20,24,27]

Here we present a homologous series of all-ring-fused ICT chromophores **1F–3F** which feature triptycene cores and π-extended, T-shaped fins. The non-iptycene **0F** has also been synthesised for comparison (Chart 1). This systematic family of molecules further informs how LUMO-homoconjugation can be utilised in multifunctional chromophore design, and also provide a powerful platform to finally explain why localising the LUMO over the core of the 3D scaffold can have such large

[a]*EaStCHEM School of Chemistry, University of Edinburgh, Joseph Black Building, David Brewster Road, Edinburgh, EH9 3FJ, UK. E-mail: iain.wright@ed.ac.uk*

[b]*Department of Chemistry, Loughborough University, Epinal Way, Loughborough, Leicestershire, LE11 3TU, UK*

[c]*Department of Chemistry, University College London, Christopher Ingold Building, London, WC1H 0AJ, UK. E-mail: tracey.clarke@ucl.ac.uk*

[d]*EPSRC Crystallographic Service, Department of Chemistry, University of Southampton, Highfield, Southampton, SO17 1BJ, UK*

[e]*Chemistry, School of Natural and Environmental Sciences, Newcastle University, Newcastle upon Tyne, NE1 7RU, UK*

[f]*School of Engineering, Physics and Mathematics, Northumbria University, Ellison Place, Newcastle upon Tyne, NE1 8ST, UK*

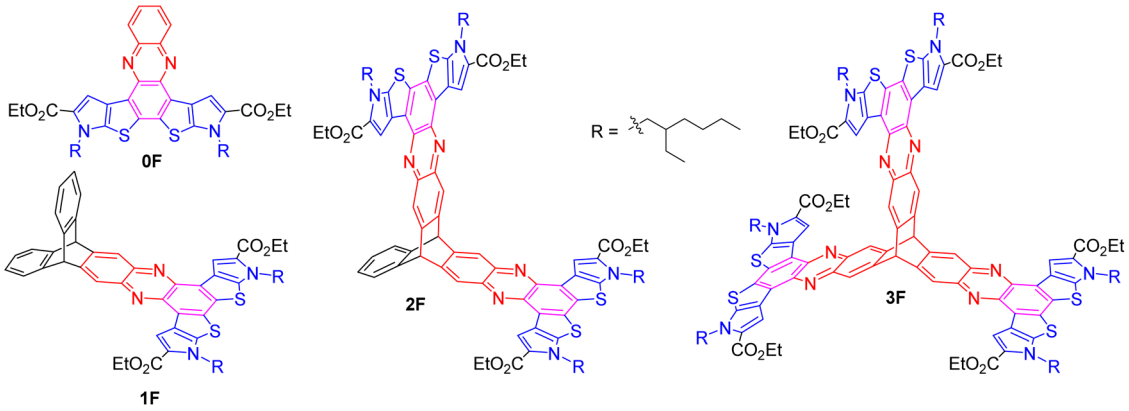

Chart 1 Molecular structures of compounds **0F–3F** (R = 2-ethylhexyl). Donor and acceptor regions are indicated in blue and red respectively. The junction aryl ring between the donor and acceptor components is indicated in magenta and is designated as Ar^{out} in the discussion.

positive effects on so many photophysical parameters in the first place.

In these new materials, the influence of homoconjugation is not identified in the low energy ICT band of the UV/vis spectra as may be expected from previous studies. Instead, it presents itself as an amplification of the molar absorbance of a progression of bands in the middle of the spectrum. These mid-spectral features of **1F–3F** display characteristics of exciton formation in a fashion which is similar in many respects to that of a classic *J*-aggregate. In fact, the properties of **1F–3F** agree very well with those of the *J*-aggregate-like model proposed by Pochas *et al.*[28] in a study which evaluated the properties of branched molecules featuring multiple pendant perylene diimide chromophores initially synthesised by Langhals *et al.*[29–31]

Supramolecular polymers have demonstrated hybrid behaviour between Frenkel exciton and intermolecular charge transfer states, leading to distinctive optical properties[32,33] and utility in photocatalysis.[34] Here, **1F–3F** further provide valuable new additions to the family of single-molecule materials, most prevalently squaraine derivatives,[35–37] which show interaction between intramolecular charge transfer and exciton states, and also complement non-ICT chromophores with 3D structures[7,38] including those which have shown promise towards singlet fission.[39–44]

The key finding here from a chromophore design standpoint is that a homoconjugated framework may be employed to separate and control distinct excitonic and ICT regimes in the UV/vis spectrum of the molecule. This provides an empowered approach to tuning the overall absorbance profile. The ability to control mid-spectral features in particular complements the absorbance-edge tuning strategies which are much more well-established.[45–47] Our new molecules also display very high fluorescence quantum yields in spite of significant SOC.

Results and discussion

Molecular design and synthesis

The molecular design was inspired by archetypical non-fullerene acceptors (NFAs) such as Y6[48] and related quinoxaline-based structures[49,50] which have intensely absorbing ICT bands at long wavelengths but comparatively weak absorbance in the mid-range. The ladder-type structure employed here utilises cross-conjugated thieno[2,3-*b*]pyrolle heterocycles and results in the outermost triply-fused aryl ring of each fin of the triptycene (Ar^{out} which is coloured magenta in Chart 1) acting as a shared junction between the electron-rich ladder regions and the electron-poor N-heterocyclic core. Ar^{out} therefore has a major contributing role in both the highest occupied molecular orbital (HOMO) and the LUMO.

The synthesis of **0F–3F** is shown in Scheme 1. Experimental procedures are in the SI. Thieno[2,3-*b*]pyrolle-5-ethylcarboxylate **1** was synthesised from ethyl azidoacetate and thiophene-3-carbaldehyde in the presence of NaOEt,[51] followed by alkylation with 2-ethylhexylbromide in the presence of K_2CO_3 to form **2**. An iridium catalysed CH-activated cross-coupling[52] with B_2pin_2 generated boronate **3** which was then homocoupled using $Pd(PPh_3)_2Cl_2$ in the presence of fluoride[53] to form **4**. Finally, direct acylation using oxalyl chloride produced the desired all ring-fused *o*-quinone **5** in modest yield. Condensation reactions to produce phenazines were then completed with 1,2-diaminobenzene and the hydrochloride salts of 2,3-diamino-,[54] 2,3,5,6-tetraamino-[55] and 2,3,5,6,11,12-hexaaminotriptycene[54] to produce **0F**, **1F**, **2F** and **3F** respectively.

X-ray crystallography

Single crystals suitable for structural determination using X-ray crystallography were obtained for **0F** and **1F** (crystal and experimental details can be found in Table S1). Despite repeated attempts, single crystals of **2F** and **3F** have not yet been obtained.

In the crystal structure of **0F** (Fig. 1) the molecules form columns in the *a*-axis direction. The columns are supported by fairly tight π-stacking interactions between the planar cores of the molecules (interplane distance 3.386 Å) resulting in a head-to-tail alignment between adjacent molecules. The columns are then arranged with interdigitation of the aliphatic groups. This interdigitation is the cause of some disorder in the chains which is not shown in Fig. 1.

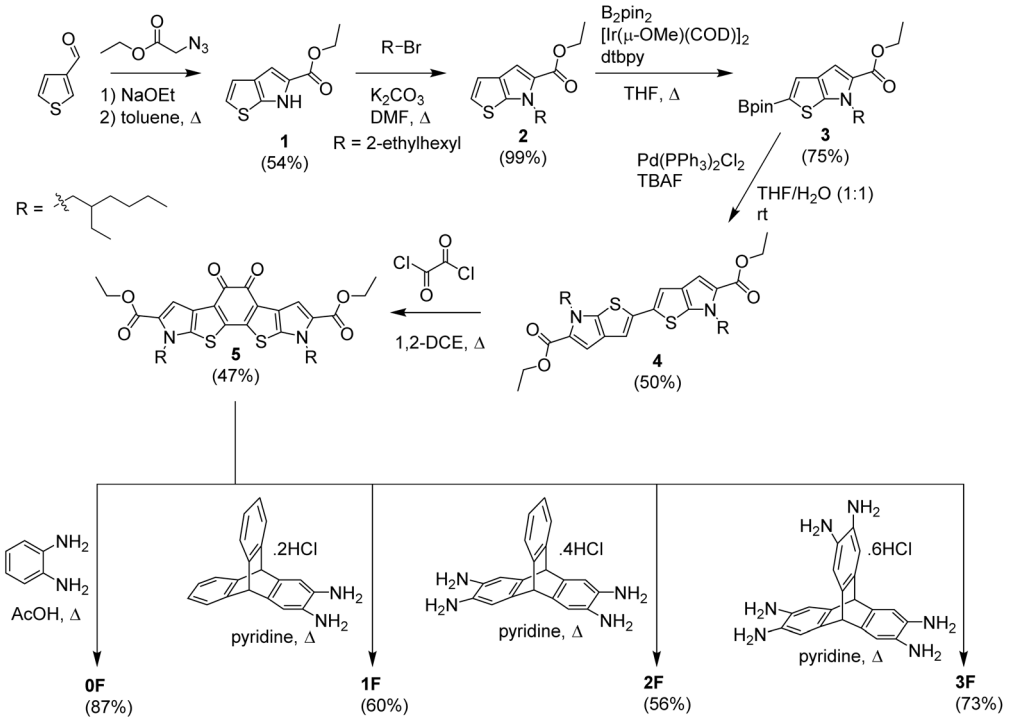

Scheme 1 Synthesis of molecules **0F–3F**.

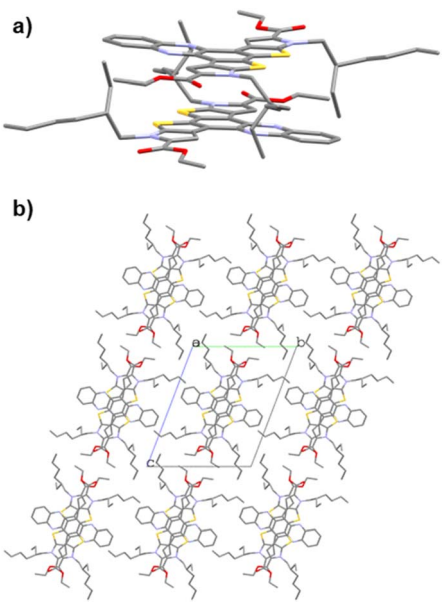

Fig. 1 X-ray crystallography determined molecular structure for **0F** showing (a) a π-stacked dimer and (b) the view down the *a*-axis. Disorder in the alkyl chains has been omitted for clarity.

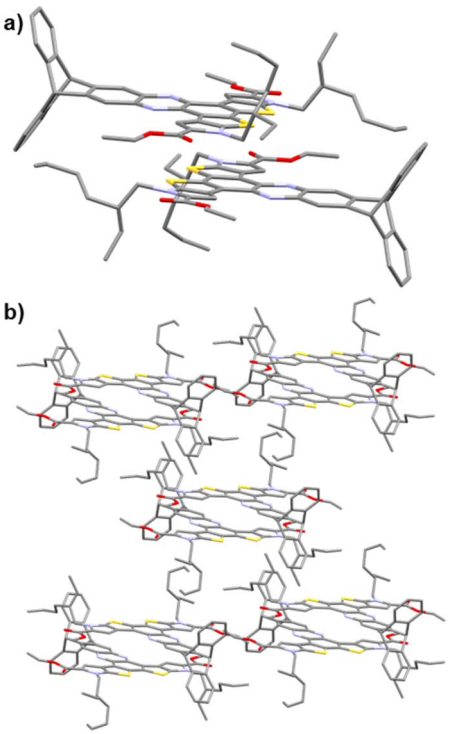

Fig. 2 X-ray crystallography determined molecular structures for **1F** showing (a) a π-stacked dimer and (b) the packing arrangement of the dimers.

The packing of **1F** (Fig. 2) has the triptycene moieties oriented towards the alkyl chain-filled regions. This results in molecules crystallising as discrete head-to-tail π-dimers. To accommodate the bulk of the triptycene moiety, the molecules in each dimer stack less directly on top of each other than in **0F**. The π-stacking distance between the **1F** molecules remains comparable to that of **0F** with an interplane distance of 3.410 Å.

Steady-state calculations

Density functional theory (DFT) optimised ground state geometries were calculated for **0F–3F** using ORCA v5 [56–58] with the

B3LYP functional, def2-TZVP basis set and def2/J auxiliary basis set.[59,60] Methyl groups were employed as substitutes for the 2-ethylhexyl chains and all geometries were true minima based on no imaginary frequencies being observed. Additional energy level values and diagrams of relevance to the following discussion can be found in the SI.

As anticipated, both the HOMO and LUMO have some density over the Ar^{out} ring for all four molecules. **0F** and **1F** (**1F** shown in Fig. 3, for **0F** see Fig. S1) have similar profiles with the HOMO localised over the cross-conjugated ladder system and the LUMO over the phenazine ring system. The slightly higher calculated HOMO and LUMO energies, and wider HOMO–LUMO gap (E_g^{calc}) for **1F** is consistent with observations made of diazaiptycenes in contrast with planar diazaacene congeners.[61]

The influence of increased dimensionality on the frontier orbital energy landscape becomes apparent in **2F** where the HOMO and HOMO−1 are now near-degenerate. The HOMO of **2F** is positioned over one functionalised fin and the HOMO−1 over the other. In contrast with **0F** and **1F** the LUMO in **2F** is spread across the entire long-axis of the molecule, straddling the homoconjugated core and leading to an orbital distribution which is reminiscent of fully conjugated benzannulated linear tetraazaacenes, albeit disrupted at the core.[62] In **3F** the presence of a third chromophore fin and the influence of the rigid, highly symmetric structure now results in degeneracy of the LUMO and LUMO+1 with each orbital covering two of the three fins. Ushiroguchi *et al.* prepared a triptycene which might be described as a tris(phenazine) fused barrelene and is therefore a good model of the core acceptor framework of **3F**. The LUMO manifold of this molecule (calculated at the B3LYP/6-31G* level) bears appropriate similarities to that of **3F** (and also **2F**) in terms of both the orbital distributions and energies.[63] Such a distribution of the LUMO suggests that constructive interplay between the fins in **2F** and **3F** might be expected. Conversely the optoelectronic properties of **0F** and **1F** should be somewhat similar to each other.

Cyclic voltammetry

Cyclic voltammetry of **0F–3F** (Fig. S3 and Table S3 with additional discussion in SI) correlated well with the DFT where all of the molecules have similar first oxidation and reduction potentials. The influence of the multiple ring systems is apparent in the reductions of **1F–3F** where the reduction scan is seen to consist of one reversible wave in **1F** then two and three overlapping waves for **2F** and **3F** respectively.

Fourier-transform Raman spectroscopy

The 3D distribution of the LUMO over adjacent fins of the triptycene core suggests that we can expect influences on the excited state properties arising from through-space effects. FT-Raman spectroscopy was therefore performed on the solid powder samples of **0F–3F**. FT-Raman is a vibrational spectroscopy technique that is very sensitive to molecular structure and conformation, so very small changes in geometry are detectable. Furthermore, because the selection rules of Raman spectroscopy require a change in electron polarizability, it also provides valuable insight into the nature of π-electron distribution in conjugated molecules,[64,65] making it well suited to understand how the homoconjugated triptycene framework interacts with the rest of the molecule.

Since the Raman spectra of large polyatomic molecules are often complex, we employed computational chemistry to enable

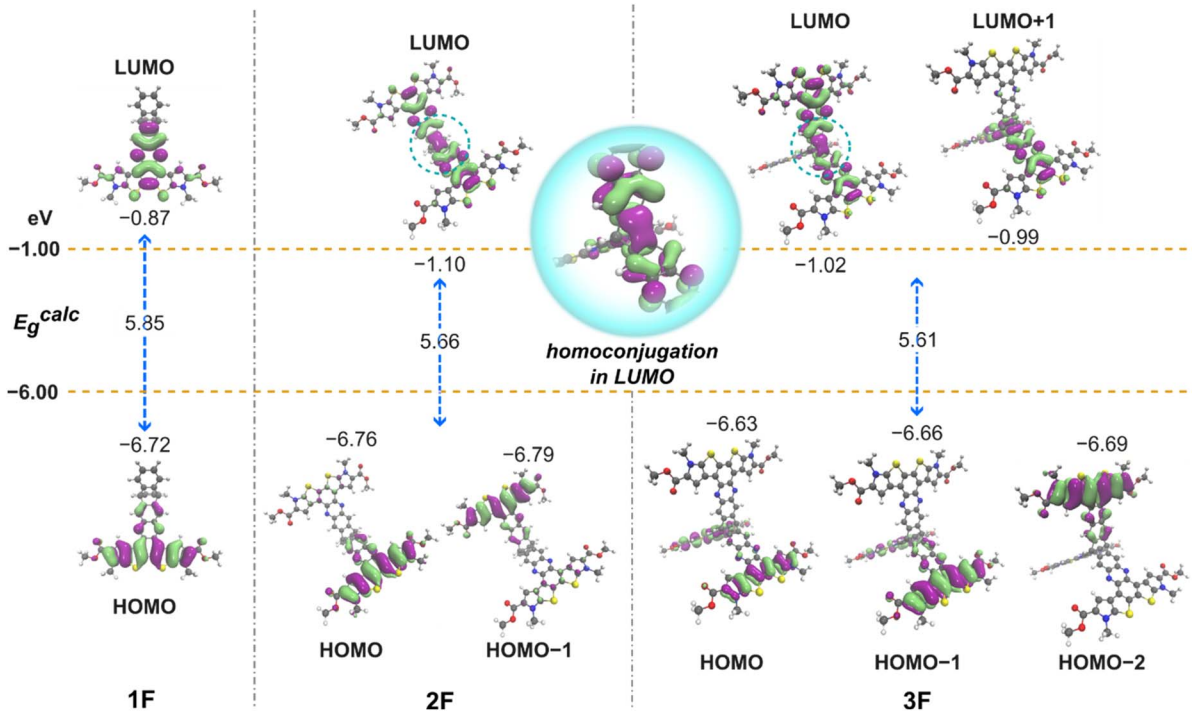

Fig. 3 Calculated (B3LYP/def2-TZVP) frontier molecular orbital distributions and energies in eV for **1F–3F**.

normal mode analysis. The calculated Raman spectra (B3LYP/6-31G(d)) are compared to the FT-Raman spectra (absence of resonance conditions) in Fig. 4 and S4. All spectra have been normalised to the C=O stretching mode at ≈1700 cm^{-1}, because this bond contributes minimally to the frontier molecular orbitals. For the purposes of the following discussion, the outermost aryl ring of the phenazine system will be designated as Ar^{out} (as described in the introduction) and the internal aryl ring (shared with the triptycene core in **1F–3F**) as Ar^{in}.

The first interesting observation from the Raman data comes from a comparison between **0F** and **1F** (Fig. 4(a)). The most intense band in the experimental spectrum for **0F** at 1417 cm^{-1} is a C=C stretching mode fully-delocalised over the thienopyrroles and the Ar^{out} ring. The same mode is upshifted in **1F** to 1429 cm^{-1}. Similarly, another delocalised C=C stretching mode is upshifted from 1393 cm^{-1} in **0F** to 1407 cm^{-1} in **1F**, and a thienopyrrole-localised C=C mode from 1539 cm^{-1} to 1546 cm^{-1}. These upshifts are also reflected in the calculated Raman spectra. The upshifts in the C=C stretching modes indicate that addition of the triptycene unit in **1F** has increased the force constant of the C=C bonds in the rest of the molecule. The observation that the fully delocalised modes have a larger upshift than the thienopyrrole-localised C=C mode suggest that it is regions of the phenazine heterocycle that possess the greatest change in bond force constant. Using the calculated bond lengths, a simple HOMA (Harmonic Oscillator Model of Aromaticity) analysis[66,67] demonstrates a large reduction in the aromaticity of Ar^{in}, with the HOMA value decreasing from 0.67 in **0F** to 0.52 in **1F** (a HOMA value of 1 represents a purely aromatic system, like benzene). This reduction in aromaticity (and subsequent upshifts in the C=C stretching modes) in **1F** arises from a subtle distortion of the Ar^{in} ring because of the adjacent triptycene core. The reduced aromaticity may cause less efficient π-conjugation and thus less intramolecular coupling between the triptycene core and the rest of the molecule in **1F**.

Next, we assess the changes in the Raman spectra as further fins are added. The comparison of **1F**, **2F**, and **3F** are presented in Fig. 4(b). Most vibrational modes show very little shift through the series. However, there are some very large differences in the experimental Raman spectra between 1445 and 1465 cm^{-1}. The weak mode at 1483 cm^{-1} in **1F** progressively downshifts to 1479 cm^{-1} then 1466 cm^{-1} for **2F** and **3F** respectively. Furthermore, the intensity of this mode increases significantly through the series. Importantly, both the increases in intensity and downshifts are replicated in the calculated Raman spectra. This vibrational mode is localised primarily over the triptycene (Fig. S4). The increase in relative intensity of this triptycene mode as the number of fins increases suggests a shift in π-electron density onto the triptycene. Furthermore, the observed downshift is consistent with enhanced π-electron delocalization and a softening of the bond force constants of the triptycene bonds' as the number of fins increases. Due to the lack of through-bond conjugation between fins, this downshift must be entirely facilitated by through-space homoconjugation.

In summary, the Raman data shows that while addition of the triptycene unit disrupts the aromaticity of the connecting quinoxaline unit in **1F**, the addition of the second and third fin in **2F** and **3F** enables homoconjugation-induced coupling between the fins, and a shift in electron density from the peripheral thienopyrrole units to the fused triptycene core.

Steady-state absorbance and emission

The steady state absorbance and emission spectra were first measured in CH_2Cl_2 (Fig. 5 and Table 1). Molar absorbance

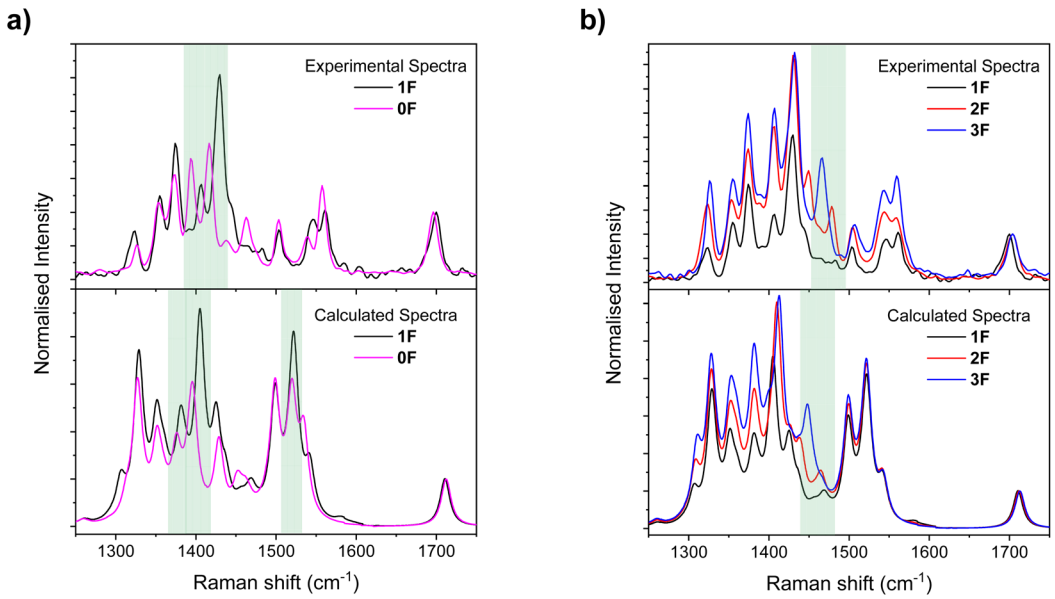

Fig. 4 FT-Raman spectra (powder, 1064 nm) and calculated Raman spectra (B3LYP/6-31G(d), frequency scaling factor 0.9613) for: (a) **0F** and **1F**. The highlighted regions indicate the vibrational modes that have upshifted from **0F** to **1F**; (b) **1F**, **2F**, and **3F**. The highlighted region indicates the triptycene-localised vibrational mode that progressively downshifts and increases in intensity from **1F** to **3F**. Data is normalised to the C=O stretching mode at ~1700 cm^{-1} in both graphs.

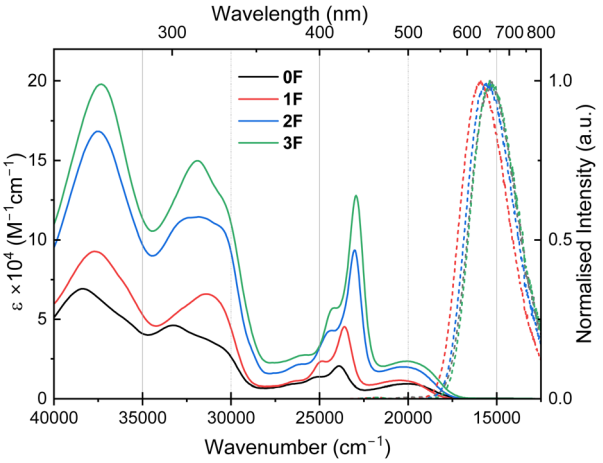

Fig. 5 Steady-state UV/vis absorbance (solid lines) and emission (dashed lines, analyte molarity = 1 μM, λ_{exc} = 500 nm) for **0F–3F** in CH_2Cl_2 solution.

coefficients were obtained using the gradient of Beer–Lambert plots (Fig. S5–S8). In contrast to the shifting profiles of the absorbance spectra (*vide infra*), the emission spectra are very similar across the series **0F–3F**. The fluorescence spectra mirror the lowest energy band of the absorbance with no fine structure. Positive solvatochromism is observed with a red-shifting of the emission frequency (ν_{em}) and increase in the Stokes shift as the solvent polarity increases (Fig. S9–S12). We can therefore conclude that the $S_1 \rightarrow S_0$ transition and the longest wavelength absorbance are of ICT character.

The limited change in the Stokes shifts of **0F–3F** in any given solvent indicates that the extent of any structural rearrangement of the system in response to the new electronic configuration is similar. This is despite the large difference in effective volume of each molecule and can be rationalised by considering the overall rigidity of the chromophore structure. The influence of the internal molecular free-volume (IMFV) of the triptycene[68,69] in precluding access of solvent molecules to the interior of the structure provides additional explanation in this respect.

Changes in the profile of the absorbance spectra of **0F–3F** are much more compelling. The spectra are composed of three distinct regions, these are intense high energy $\pi \rightarrow \pi^*$ transitions above 27 500 cm^{-1} followed by a systematic series of peaks (ν_{MID}) in the middle of the spectrum with a longest wavelength absorbance (ν_{MID1}) in the range of 23 000–24 000 cm^{-1}. Finally, there is a broad ICT band (ν_{ICT}) in the range of 20 000–20 500 cm^{-1}. We note that **0F** has both the shortest ν_{mid} and the longest ν_{ICT}, indicative of slightly stronger dipolar character leading to an optical HOMO–LUMO gap (E_g^{opt}) which is comparable to that of **2F**.

First, we compare **0F** and **1F**. The only structural difference between **0F** and **1F** is the presence of the homoconjugated dibenzobarrelene moiety fused onto the end of **1F**. It would be reasonable to expect the spectra of these molecules to be extremely similar. Indeed the ν_{ICT} and ν_{MID} of **1F** are only slightly blueshifted and redshifted respectively and ε_{ICT} in **1F** is also comparable to that of **0F**. However, a stark difference is observed in ε_{MID} which more than doubles in intensity from 20.5 × 10^3 M^{-1} cm^{-1} (**0F**) to 45.2 × 10^3 M^{-1} cm^{-1} (**1F**).

Upon comparing between the triptycene-based compounds **1F–3F** more systematic variations in the peak positions and intensities can be discerned. ν_{MID1} redshifts by 543 cm^{-1} moving from **1F** to **2F** but then only 106 cm^{-1} from **2F** to **3F**. In contrast ν_{ICT} redshifts in a step-like fashion by approximately 200 cm^{-1} upon addition of each subsequent fin. Examining the peak intensities, ε_{MID} more than doubles moving from **1F** (45.2 × 10^3 M^{-1} cm^{-1}) to **2F** (93.5 × 10^3 M^{-1} cm^{-1}) followed by a smaller but still large, increase of 34.4 M^{-1} cm^{-1} in **3F** (127.9 × 10^3 M^{-1} cm^{-1}). The intensity of the higher energy $\pi \rightarrow \pi^*$ transitions also increase in a similar manner to the ν_{MID} bands.

To better understand the transitions involved at ν_{MID} and ν_{ICT} calculations were performed using DFT and linear response time-dependent DFT (LR-TDDFT) within the approximation of the optimally tuned LC-BLYP exchange and correlation functional. A def2-TZVP basis set was used throughout and the solvent assumed to be toluene.

Difference plots (Fig. 6) confirmed that ν_{ICT} pertains to the singlet $S_1 \rightarrow S_0$ transition from the donor ladder-region(s) into the acceptor phenazine(s). In **2F** and **3F** there is some MO density spread over two of the fins which suggests the possibility of multiple fins being excited directly into the ICT state simultaneously is unlikely. The calculations confirm that ν_{MID} is a $\pi \rightarrow \pi^*$ transition occurring to progressively higher (but isoenergetic) singlet excited states as the number of functional fins increases. This is exemplified by S_3 for both **0F** and **1F**, S_5 for **2F** and S_7 for **3F**. Large clusters of low energy triplet states are also observed, with the number of low-lying triplet states increasing with the number of fins on the triptycene (Fig. S2 and Table S2).

Table 1 Steady-state absorbance and emission properties of **0F–3F** in CH_2Cl_2 solution

	ν_{MID} (cm^{-1}) [ε_{MID} × 10^3 M^{-1} cm^{-1}]						
	ν_{MID1}	ν_{MID2}	ν_{MID3}	ν_{ICT} (cm^{-1}) [ε_{ICT} × 10^3 M^{-1} cm^{-1}]	ν_{em}[a] (cm^{-1})	Stokes shift (cm^{-1}) [eV]	E_g^{opt}[b] (eV)
0F	23 923 [20.5]	25 062 [13.8]	26 315 [9.3]	20 049 [9.3]	15 369	4680 [0.58]	2.18
1F	23 584 [45.2]	24 846 [23.5]	26 134 [11.3]	20 470 [11.5]	15 978	4492 [0.57]	2.23
2F	23 041 [93.5]	24 330 [42.9]	25 965 [21.6]	20 283 [19.8]	15.640	4643 [0.58]	2.18
3F	22 935 [127.9]	24 154 [57.1]	25 610 [27.4]	20 060 [23.5]	15 384	4676 [0.58]	2.15

[a] Analyte molarity = 1 μM, (λ_{exc} = 500 nm). [b] Optical HOMO–LUMO gap calculated from the onset of absorbance according to: $E_g^{opt} = 1240.68 \times (\nu_{onset} \times 10^{-7})$.

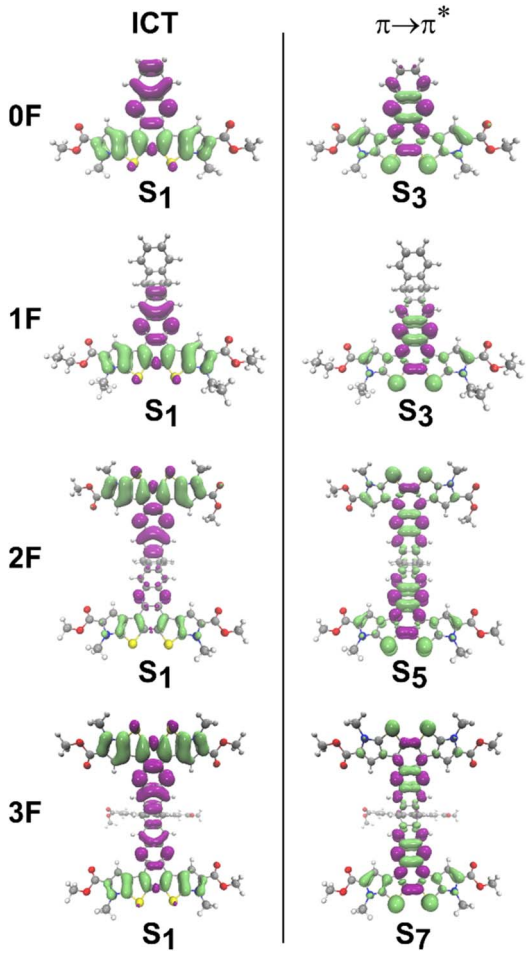

Fig. 6 TDDFT calculated difference plots for the $S_0 \rightarrow S_1$ transitions associated with ν_{ICT} and the transitions to higher singlet states associated with ν_{MID} (colours: green = electron, magenta = hole).

Understanding homoconjugation-induced enhancements in optical properties of triptycenes

The overall change observed across the ν_{MID} progression of peaks is a stepwise but non-linear increase in ε upon addition of subsequent fins. This is similar to those observed for dye aggregates as described by the exciton model pioneered by Kasha.[70] The electronic structure of an aggregate is dictated by the relative positions of its composite molecules. The model has been extended successfully to several multi-chromophore systems and even conjugated polymers.[2] In its earliest iterations, it was used to explain the spectroscopic properties of homoconjugated molecules diphenylmethane and triphenylmethane and also much more rigid V-shaped molecules such as Tröger's base.[70] In the context of triptycenes, exciton coupling has previously been invoked to explain aspects of the optical properties of *E*/*Z* photoisomerising azobenzene substituted triptycenes.[71]

The two classes of aggregate considered most frequently are intermolecular *J*- and *H*-aggregates between entirely (or largely) planar molecules such as perylene diimides (PDIs)[8,72–74] and merocyanines.[75] Upon examination of initial experimental studies by Langhals and co-workers on star-like multi-chromophore systems,[29–31,76] Pochas *et al.* established that a symmetrical trimeric complex of PDIs held in a trefoil configuration has its own distinct exciton properties classed as neither a *J*- nor *H*-aggregate.[28] This trefoil structure has a topology similar to that of triptycene so provides an excellent basis by which to understand the variations observed in the ν_{MID} portion of the UV/vis spectra between **1F–3F**.

The exciton model posits that the transition dipole moment (M) in Debye (D) of the aggregate should scale according to square root of the number of monomers (N). Normally in the study of aggregate dyes, the long wavelength edge of the absorbance spectra can conveniently be used to extract M^{Abs}. However, for the molecules presented here, the low energy features of the UV/vis are entirely ICT in nature and any exciton-induced enhancements are being observed in the middle of the spectrum.

To overcome this, the entire spectrum was integrated (Fig. 7(a)) and the integrands of both the highest intensity peak of ν_{MID1} and the entire ICT band ν_{ICT} were used in eqn (1) (where n is the refractive index, $n = 1.424$ for CH_2Cl_2 (ref. 77) and ν is

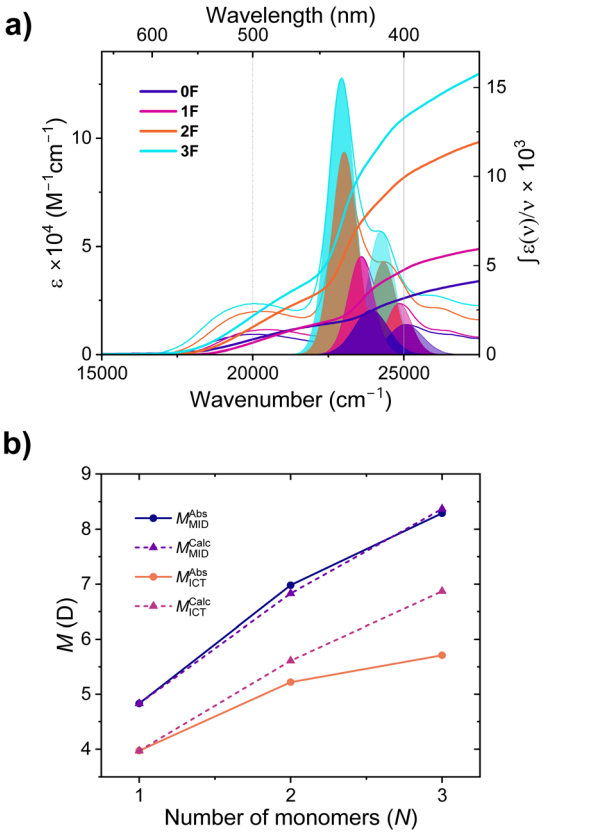

Fig. 7 (a) UV/vis absorbance spectrum (left-hand axis) of **0F–3F** in CH_2Cl_2 solution overlaid with the integral of ε/ν (right hand axis) which was then used to calculate the experimental transition dipole moments M_{ICT}^{Abs} and M_{MID}^{Abs} and also showing the Gaussian peak fittings (shaded peaks) used to calculate S_{AN}. (b) A close agreement is observed for ν_{MID} between the experimentally determined transition dipole moments compared to those predicted from the exciton model.

Table 2 Experimental transition dipole moments (M_{MID}^{Abs} and M_{ICT}^{Abs}) for **0F–3F**, the S_{AN} and R_{abs} values for **1F–3F** and the calculated transition dipole moments (M_{MID}^{Calc} and M_{ICT}^{Calc}) for **1F–3F**

		Experimental values				Calculated values	
	N	M_{MID}^{Abs}(D)^a [f_{osc}]^b	M_{ICT}^{Abs}(D)^a [f_{osc}]^b	S_{AN}	R_{abs}	M_{MID}^{Calc}(D)^c	M_{ICT}^{Calc}(D)^d
0F	—	3.50 [0.14]	3.93 [0.15]	—	—	—	—
1F	1	4.83 [0.26]	3.97 [0.15]	1.00	1.92	4.83	3.97
2F	2	6.98 [0.53]	5.22 [0.26]	1.05	2.18	6.83	5.61
3F	3	8.29 [0.74]	5.71 [0.31]	0.99	2.23	8.37	6.87

^{a} Calculated according to eqn (1). ^{b} Calculated according to eqn (2). ^{c} Calculated as the product of $\sqrt{N}$ (where N is the number of monomers) and M_{MID}^{Abs} of **1F** as the monomer. ^{d} Calculated as the product of $\sqrt{N}$ (where N is the number of monomers) and M_{ICT}^{Abs} of **1F** as the monomer. ^{d} An updated Table 2 was attached in response to Q4.

the wavenumber in cm^{-1}) to calculate the transition dipole moment for the absorbance bands ν_{MID1} and ν_{ICT} to obtain M_{MID}^{Abs} and M_{ICT}^{Abs} respectively (Table 2).[78] The lowest energy points on either side of the peaks in question were taken as the limits of integration.

$$M^{Abs} = 9.58 \times 10^{-2}\left(\frac{(2n^2+1)^2}{9n^3} \times \int \frac{\varepsilon(\nu)}{\nu} d\nu\right)^{1/2} \quad (1)$$

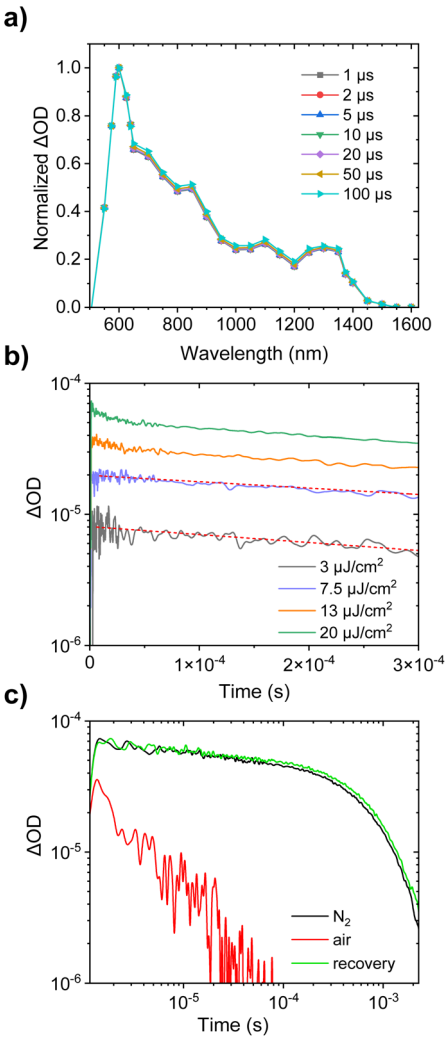

Fig. 8 (a) Normalised TA spectra of **3F** (toluene) solution, excited at 415 nm, 20 μJ cm^{-2}, (b) energy dependence of **3F** (toluene) solution, excited at 415 nm, probed at 700 nm (c) Reversible oxygen quenching of the long-lived decay component of **3F**.

Again, we first compare **0F** and **1F**. Their values of M_{ICT}^{Abs} are found to be very similar but M_{MID}^{Abs} are significantly different. That there is a difference at all further demonstrates that the triptycene-framework is not an innocent bystander in the optoelectronic properties of these materials. From this we can draw an initial important conclusion which is that **1F** is a more appropriate molecule to consider as the monomer ($N = 1$) for comparison with the dimeric and trimeric "aggregates" **2F** ($N = 2$) and **3F** ($N = 3$). This observation also suggests that the preparation of **1F**-like triptycene-fused molecules will be much more informative than non-triptycene **0F**-like homologues as model compounds for any **2F**- or **3F**-like systems.

The experimental values of M_{MID}^{Abs} and M_{ICT}^{Abs} obtained for **1F** were then scaled by $\sqrt{N}$ to obtain calculated values M_{MID}^{Calc} and M_{ICT}^{Calc} for **1F–3F** (Fig. 7(b) and Table 3). The experimental and calculated values for M_{MID} are in excellent agreement while those for M_{ICT} are not. The absence of $\sqrt{N}$ scaling for μ_{CT} suggests that exciton interactions are only occurring upon population of the higher excited states represented by ν_{MID}. Trends in the variation of M_{ICT} for **1F–3F** arise from the incremental increase in acceptor strength as further pyrazine rings are fused onto the triptycene.

Oscillator strengths (f_{osc}) for the ν_{MID} and ν_{ICT} transitions were subsequently calculated using eqn (2) and were included in Table 1.[79]

$$f_{ocs} = 4.702 \times 10^{-7}\nu|M^{Abs}|^2 \quad (2)$$

The variation in f_{osc} with respect to N is also consistent with Pochas' model. The f_{osc} is enhanced relative to that of the monomer in each case, but the extent of enhancement decreases as N increases. For a true J-aggregate the extent of enhancement should increase with N. It is also observed that the areas of Gaussian peaks fitted to the ν_{MID1} for **2F** and **3F** scale to a decreasing number of N times the monomer area as N increases. This is expressed as the ratio S_{AN} and is equal to 1.05

Table 3 Photophysical properties of **0F–3F** in dilute toluene solution

	E_{S1} (eV)	ϕ_f (%)	τ_f (ns)	k_r (10^7 s^{-1})	k_{nr} (10^7 s^{-1})	τ_T (μs)	M_{ICT}^{em}(D)[a]
0F	2.25	66 ± 4	18.0	3.7 ± 0.2	1.9 ± 0.2	740 ± 140	2.74
1F	2.32	75 ± 10	18.0	4.2 ± 0.6	1.4 ± 0.6	880 ± 140	2.78
2F	2.27	68 ± 12	19.7	3.5 ± 0.7	1.6 ± 0.6	570 ± 40	2.63
3F	2.23	86 ± 12	20.6	4.2 ± 0.6	0.7 ± 0.6	790 ± 90	2.94

[a] Calculated using eqn (3).

and 0.99 for **2F** and **3F** respectively. The ν_{MID1} peak redshifts with increasing N and the ratio of f_{osc} of the ν_{MID1} and ν_{MID2} bands (R_{abs}) increases with N.

Overall, these observations demonstrate generality to the exciton model proposed for a trefoil system, which agrees very well with the ν_{MID} region for **1F–3F**. Any deviations from this model are minor and due to structural differences imposed by the triptycene core when compared to the PDI model systems. These include rigid 120° angles between the planes of the chromophores, and the fact that any twisting between the chromophores is no longer possible. This finally provides some explanation for super-summative enhancements which have previously been observed in triptycene based materials, and reveals a new approach to tuning the mid-spectral profile of functional chromophores.

Time-resolved photophysics

Finally, we turn our attention to understanding the excited state properties through time-resolved methods. Due to the low boiling point of CH_2Cl_2, and requirement to exclude oxygen *via* freeze–pump–thaw methods, toluene was adopted as an appropriate solvent from which to obtain the time-resolved measurements.

The fluorescence photoluminescence quantum yield (Φ_f), fluorescence lifetime (τ_{fl}), radiative decay rates (k_r) and non-radiative decay rates (k_{nr}) are shown in Table 3. Φ_f was high for all of the compounds, most notably for the largest molecule **3F** with a value of 86 ± 12% which is comparable with some of the most strongly emitting superradiant *J*-aggregates.[80–83] The relative differences with **1F** and **2F** indicate that the core of the high-symmetry structure **3F** is well-shielded from the external solution thereby circumventing intermolecular loss pathways. The planar structure of **0F** permits more direct comparison with other dithienophenazines. In general, chromophores based around this ring-system display low Φ_f (typically 0.5–10%)[84–86] in solution with a handful of examples having Φ_f >10% (ref. 87 and 88) so **0F** is notably luminescent in any case.

To complement the analysis of the UV/vis spectra (*vide supra*) transition dipole moments of the ICT emission band (M_{ICT}^{em}) were calculated using k_r and the emission wavenumber ν_{em} according to eqn (3) (ref. 89) (note that this equation requires use of the Planck constant in $h = 6.626 \times 10^{-27}$ erg s and upon solving for M a conversion factor of 10^{18} must be applied to convert from statC.cm to Debye, for toluene $n = 1.497$ (ref. 76)). This gave similar results across the series and had values consistent with ICT emission which again supports the idea of a common radiative deactivation pathway for **0F–3F**.

$$k_r = \frac{64\pi^4}{3h} n^3 \nu_{em}{}^3 \left| M_{ICT}^{em} \right|^2 \quad (3)$$

The singlet lifetimes of **0F** and **1F** are identical but τ_{fl} then gets incrementally longer moving to **2F** and **3F**. This may seem surprising as the radiative lifetime of the aggregate should decrease with increasing N.[2,80,81,90] We rationalise this by considering that, as the radiative step is occurring through the ICT state S_1, increasingly fast internal conversion may well be occurring from the ν_{MID} exciton manifold into S_1 but the overall rate of emission is then effectively throttled by the k_r of the ICT state. The identical lifetimes of **0F** and **1F** support this hypothesis. The extracted k_r values are therefore also rather similar across the series **0F–3F** in the range of 3–5 × 10^7 s^{-1}. The k_{nr} values are quite similar for **0F–2F** but that of **3F** appears to be meaningfully slower. Since high k_{nr} is detrimental to OPV performance,[91,92] this suggests that further development of this design concept may lead to promising NFA materials.

Finally, transient absorbance spectroscopy (TAS) was employed to identify triplet formation in **0F–3F** with a view to explaining the dense manifolds of low-lying triplet states and significant spin–orbit coupling (SOC) induced intersystem crossing (ISC) which have previously been observed in ICT iptycenes.

Unfortunately, due to the intense emission of the molecules which persist for longer than the interval between TA pump pulses, potentially crucial insight into the triplet formation could not be obtained from ps-TAS measurements. However, as the τ_{fl} of the materials are on the order of tens of ns, such intense emission did not present an issue in obtaining μs-TAS. All four molecules show similar μs-TA spectra: a strong band at 600 nm with vibronic structure and a weaker band at 1300 nm, as exemplified for **3F** in Fig. 8 (the relevant plots for **0F–2F** can be found in Fig. S13–S15). The 600 nm band is very close to the negative ground state bleach (GSB) region which may obscure its true position and intensity. Note that the μs-TA spectra excited at 415 nm (ν_{MID}) and 500 nm (ν_{ICT}) exhibit similar shapes and intensities. There is no significant spectral evolution in any of the samples, which strongly suggests that both 600 nm and 1300 nm bands can be attributed to only one type of transient species. For all four molecules, the kinetics at low fluences (3–7 μJ cm^{-2}) are monoexponential, which is characteristic of triplet excitons on these timescales. Second-order processes (such as exciton–exciton annihilation) at early times are apparent at higher fluences. Oxygen-dependent

measurements revealed strong but reversible oxygen quenching of the TA signal, both in terms of intensity and lifetime. This confirms the presence of triplets in all of the solutions.

The 7.5 μJ cm^{-2} data was used to compare the decay kinetics between the different samples, as it exhibits the best signal-to-noise ratio without showing any second order effects. The triplet lifetimes were estimated (Table 3) and are quite similar across the series (Fig. S16). This suggests that similar triplet decay pathways are present in each molecule, consistent with their similar energetics and similar fluorescence properties. While the TAS suggests some triplet populations forming under excitation at 415 nm as supported by the TDDFT, the rapid k_r and high Φ_f of the molecules suggests that fast internal conversion to S_1 followed by fluorescence is the predominant relaxation pathway. The ISC occurring into triplet states, especially from the higher singlet states, will be a minor pathway.

Concerning the origin of the SOC enhancements which are facilitating the ISC observed in ICT-triptycenes, the spin–orbit, charge-transfer intersystem crossing (SOCT-ISC)[77,93–95] mechanism has previously been invoked to explain similar observations in related V-shaped molecules,[96] and slip-stacked dimers of PDIs which also demonstrate excitonic effects.[97] Also, the fin structure is built around phenazine which itself is an effective triplet sensitiser[98] arising from mixing of the S_1 n → π* and T_1 π → π* states in accordance with El-Sayed's rule.[99,100] It is likely that a combination of both factors are at play in these molecules.

Conclusions

To conclude, we have presented a systematic series of triptycene-based homoconjugated chromophores **0F–3F** which show an interplay between a low energy ICT transition and a sequence of π → π* transitions which are located in the middle of the absorption spectrum. The variations in intensity and position of the mid-spectrum are described well as an intramolecular exciton state. This has finally provided an explanation for the enhancements in various photophysical properties observed in LUMO-homoconjugated chromophores. It seems likely that this is a general phenomenon for this class of material.

These new molecules are also highly fluorescent with **3F** having a near-unity photoluminescence quantum yield within experimental error. The results obtained suggest that intramolecular loss mechanisms through the triplet manifold in **3F** are circumvented by very rapid internal conversion from higher singlet states to S_1 prior to radiative decay through the ICT channel. Collisional deactivation is also decreased by its bulky, well-shielded structure leading to very efficient luminescence overall. This provides an important contrast with existing studies concerning the modulation of ICT between distinct donor and acceptor fins.[17,101–105]

The key findings of separation between the excitonic and ICT regimes reveals new structure-property relationships to be explored. These features should be independently tunable so the ICT band can be shifted or rendered more intense using the typical band-edge tuning strategies, while the exciton progression can be similarly tuned through modifications at the triptycene core. Benefits that might be realised by harnessing the distinct photophysical behaviour of exciton and ICT states simultaneously in a single molecule include circumventing non-radiative decay efficiency losses in low energy gap emitters for OLEDs and bioimaging,[106–108] the ability to maximise the efficiency of broadband absorbance while avoiding triplet-mediated loss mechanisms in organic solar cell materials,[109] and straightforward colour tuning and dissymmetry factor enhancement in chiroptical materials,[32] rendering this an empowered approach to new functional chromophore design.

Author contributions

I. A. W. conceptualised the research. S. W. synthesised the molecules and completed the electrochemistry and steady-state absorbance spectroscopy. H. I. G. and T. M. C. performed the Raman and time-resolved spectroscopy. G. S. N., E. M. D. & S. J. C. completed the X-ray crystallography. T. J. P. conducted the computational analysis. M. K. E. completed photoluminescence and additional steady-state absorbance spectroscopy. I. A. W. and T. M. C. wrote the manuscript. All authors contributed to discussing the results obtained and commenting on the manuscript.

Conflicts of interest

There are no conflicts to declare.

Data availability

CCDC 2495341 (**0F**) and 2502203 (**1F**) contain the supplementary crystallographic data for this paper.[111a,b]

The data required to form the conclusions of this study are present in the paper itself, or are included in the supplementary information (SI). Additional data can be provided by the corresponding author(s) upon request. Supplementary information is available. See DOI: https://doi.org/10.1039/d6sc01073c.

Acknowledgements

I. A. W. and S. W. acknowledge financial support from EPSRC grant EP/T028688/2. We also acknowledge EP/X035174/1 (EPSRC) and BB/X019756/1 (BBSRC) for NMR instrumentation. T. M. C. and H. I. G. acknowledge financial support from EPSRC grants EP/N509577/1 and EP/T517793/1. T. J. P. acknowledges the EPSRC for an Open Fellowship (EP/W008009/1) and COSMOS Programme grant (EPSRC grant no. EP/X026973/1). M. K. E acknowledges The Royal Society for funding (RG\R1\251201). This research made use of the Rocket High Performance Computing service at Newcastle University and computational resources from ARCHER2 UK National Computing Service which was granted *via* HPC–CONEXS, the UK High-End Computing Consortium (EPSRC grant no. EP/X035514/1). We thank the EPSRC UK National Crystallography Service at the University of Southampton for the collection of the crystallographic data.[110]

References

1 A. L. Kanibolotsky, I. F. Perepichka and P. J. Skabara, *Chem. Soc. Rev.*, 2010, **39**, 2695.
2 N. J. Hestand and F. C. Spano, *Chem. Rev.*, 2018, **118**, 7069.
3 P. Parkinson, D. V. Kondratuk, C. Menelaou, J. Q. Gong, H. L. Anderson and L. M. Herz, *J. Phys. Chem. Lett.*, 2014, **5**, 4356.
4 T. Brixner, R. Hildner, J. Köhler, C. Lambert and F. Würthner, *Adv. Energy Mater.*, 2017, **7**, 1700236.
5 G. D. Scholes and K. P. Ghiggino, *J. Phys. Chem.*, 2002, **98**, 4580.
6 G. Zhang, V. Lami, F. Rominger, Y. Vaynzof and M. Mastalerz, *Angew. Chem., Int. Ed.*, 2016, **128**, 4045.
7 L. Lv, W. Sun, Z. Jia, G. Zhang, F. Wang, Z. a. Tan and L. Zhang, *Mater. Chem. Front.*, 2020, **4**, 3539.
8 C. Ramanan, C. H. Kim, T. J. Marks and M. R. Wasielewski, *J. Phys. Chem. C*, 2014, **118**, 16941.
9 H. Yoo, S. Furumaki, J. Yang, J. E. Lee, H. Chung, T. Oba, H. Kobayashi, B. Rybtchinski, T. M. Wilson, M. R. Wasielewski, M. Vacha and D. Kim, *J. Phys. Chem. B*, 2012, **116**, 12878.
10 Q. Wu, D. Zhao, J. Yang, V. Sharapov, Z. Cai, L. Li, N. Zhang, A. Neshchadin, W. Chen and L. Yu, *Chem. Mater.*, 2017, **29**, 1127.
11 E. H. Menke, V. Lami, Y. Vaynzof and M. Mastalerz, *Chem. Commun.*, 2016, **52**, 1048.
12 S. R. Peurifoy, E. Castro, F. Liu, X. Y. Zhu, F. Ng, S. Jockusch, M. L. Steigerwald, L. Echegoyen, C. Nuckolls and T. J. Sisto, *J. Am. Chem. Soc.*, 2018, **140**, 9341.
13 J. Zhang, Y. Li, J. Huang, H. Hu, G. Zhang, T. Ma, P. C. Y. Chow, H. Ade, D. Pan and H. Yan, *J. Am. Chem. Soc.*, 2017, **139**, 16092.
14 D. Meng, H. Fu, C. Xiao, X. Meng, T. Winands, W. Ma, W. Wei, B. Fan, L. Huo, N. L. Doltsinis, Y. Li, Y. Sun and Z. Wang, *J. Am. Chem. Soc.*, 2016, **138**, 10184.
15 J. W. Lee, J. S. Park, H. Jeon, S. Lee, D. Jeong, C. Lee, Y. H. Kim and B. J. Kim, *Chem. Soc. Rev.*, 2024, **53**, 4674.
16 H. Yu, L. Arunagiri, L. Zhang, J. Huang, W. Ma, J. Zhang and H. Yan, *J. Mater. Chem. A*, 2020, **8**, 6501.
17 K. Kawasumi, T. Wu, T. Zhu, H. S. Chae, T. Van Voorhis, M. A. Baldo and T. M. Swager, *J. Am. Chem. Soc.*, 2015, **137**, 11908.
18 S. Kumar, L. G. Franca, K. Stavrou, E. Crovini, D. B. Cordes, A. M. Z. Slawin, A. P. Monkman and E. Zysman-Colman, *J. Phys. Chem. Lett.*, 2021, **12**, 2820.
19 K. Madhusudana Rao, R. Ramaraghavulu, D. Kolli, S. H. Babu and S. V. P. Vattikuti, *J. Mater. Chem. C*, 2025, **13**, 3091.
20 S. Montanaro, P. Pander, J.-R. Mistry, M. R. J. Elsegood, S. J. Teat, A. D. Bond, I. A. Wright, D. G. Congrave and M. K. Etherington, *J. Mater. Chem. C*, 2022, **10**, 6306.
21 X. Tang, L. S. Cui, H. C. Li, A. J. Gillett, F. Auras, Y. K. Qu, C. Zhong, S. T. E. Jones, Z. Q. Jiang, R. H. Friend and L.-S. Liao, *Nat. Mater.*, 2020, **19**, 1332.
22 E. Spuling, N. Sharma, I. D. W. Samuel, E. Zysman-Colman and S. Bräse, *Chem. Commun.*, 2018, **54**, 9278.
23 M. Yu, X. Zhu, J. Zeng, H. Liu, R. Huang, Z. Zhuang, P. Shen, Z. Zhao and B. Z. Tang, *J. Mater. Chem. C*, 2021, **9**, 14808.
24 J.-R. Mistry, S. Montanaro and I. A. Wright, *Mater. Adv.*, 2023, **4**, 787.
25 See: https://goldbook.iupac.org/terms/view/H02842.
26 P. Muller, *Pure Appl. Chem.*, 1994, **66**, 1077.
27 S. Montanaro, D. G. Congrave, M. K. Etherington and I. A. Wright, *J. Mater. Chem. C*, 2019, **7**, 12886.
28 C. M. Pochas, K. A. Kistler, H. Yamagata, S. Matsika and F. C. Spano, *J. Am. Chem. Soc.*, 2013, **135**, 3056.
29 H. Langhals and J. Gold, *J. Prakt. Chem./Chem.- Ztg.*, 1996, **338**, 654.
30 H. Langhals, C. Wagner and R. Ismael, *New J. Chem.*, 2001, **25**, 1047.
31 H. Langhals, *Helv. Chim. Acta*, 2005, **88**, 1309.
32 J. Han, S. Fujikawa and N. Kimizuka, *Angew. Chem., Int. Ed.*, 2024, **63**, e202410431.
33 M. Wehner, M. I. S. Rohr, M. Buhler, V. Stepanenko, W. Wagner and F. Würthner, *J. Am. Chem. Soc.*, 2019, **141**, 6092.
34 N. J. Hestand, R. V. Kazantsev, A. S. Weingarten, L. C. Palmer, S. I. Stupp and F. C. Spano, *J. Am. Chem. Soc.*, 2016, **138**, 11762.
35 T. Maeda, T. V. Nguyen, Y. Kuwano, X. Chen, K. Miyanaga and H. Nakazumi, *J. Phys. Chem. C*, 2018, **122**, 21745.
36 C. Lambert, J. Hoche, M. H. Schreck, M. Holzapfel, A. Schmiedel, J. Selby, A. Turkin and R. Mitric, *J. Phys. Chem. A*, 2021, **125**, 2504.
37 H. Ceymann, M. Balkenhohl, A. Schmiedel, M. Holzapfel and C. Lambert, *Phys. Chem. Chem. Phys.*, 2016, **18**, 2646.
38 G. D. Scholes, K. P. Ghiggino, A. M. Oliver and M. N. Paddon-Row, *J. Am. Chem. Soc.*, 2002, **115**, 4345.
39 L. Ahrens, N. Wollscheid, J. Han, O. Kefer, F. Rominger, A. Roozbeh, J. Freudenberg, A. Dreuw, U. H. F. Bunz and T. Buckup, *J. Phys. Chem. B*, 2021, **125**, 13235.
40 J. D. Cook, T. J. Carey, D. H. Arias, J. C. Johnson and N. H. Damrauer, *J. Phys. Chem. A*, 2017, **121**, 9229.
41 N. V. Korovina, S. Das, Z. Nett, X. Feng, J. Joy, R. Haiges, A. I. Krylov, S. E. Bradforth and M. E. Thompson, *J. Am. Chem. Soc.*, 2016, **138**, 617.
42 K. C. Krishnapriya, A. J. Musser and S. Patil, *ACS Energy Lett.*, 2018, **4**, 192.
43 E. Kumarasamy, S. N. Sanders, M. J. Y. Tayebjee, A. Asadpoordarvish, T. J. H. Hele, E. G. Fuemmeler, A. B. Pun, L. M. Yablon, J. Z. Low, D. W. Paley, J. C. Dean, B. Choi, G. D. Scholes, M. L. Steigerwald, N. Ananth, D. R. McCarney, M. Y. Sfeir and L. M. Campos, *J. Am. Chem. Soc.*, 2017, **139**, 12488.
44 M. R. Rapp, R. Weiß, A. S. Wollny, D. M. Guldi and H. F. Bettinger, *Adv. Funct. Mater.*, 2024, **34**, 2313576.
45 D. F. Perepichka and M. R. Bryce, *Angew. Chem., Int. Ed.*, 2005, **44**, 5370.
46 D. Hashemi, X. Ma, R. Ansari and J. Kim, *Phys. Chem. Chem. Phys.*, 2019, **21**, 789.

47 L. Dou, Y. Liu, Z. Hong, G. Li and Y. Yang, *Chem. Rev.*, 2015, **115**, 12633.
48 J. Yuan, Y. Zhang, L. Zhou, G. Zhang, H.-L. Yip, T.-K. Lau, X. Lu, C. Zhu, H. Peng, P. A. Johnson, M. Leclerc, Y. Cao, J. Ulanski, Y. Li and Y. Zou, *Joule*, 2019, **3**, 1140.
49 Z. Zhou, W. Liu, G. Zhou, M. Zhang, D. Qian, J. Zhang, S. Chen, S. Xu, C. Yang, F. Gao, H. Zhu, F. Liu and X. Zhu, *Adv. Mater.*, 2020, **32**, e1906324.
50 H. Chen, H. Liang, Z. Guo, Y. Zhu, Z. Zhang, Z. Li, X. Cao, H. Wang, W. Feng, Y. Zou, L. Meng, X. Xu, B. Kan, C. Li, Z. Yao, X. Wan, Z. Ma and Y. Chen, *Angew. Chem., Int. Ed.*, 2022, **61**, e202209580.
51 A. Vogt, F. Henne, C. Wetzel, E. Mena-Osteritz and P. Bauerle, *Beilstein J. Org. Chem.*, 2020, **16**, 2636.
52 D. W. Robbins and J. F. Hartwig, *Org. Lett.*, 2012, **14**, 4266.
53 M. G. Finn, S. Punna and D. D. Díaz, *Synlett*, 2004, **17**, 2351.
54 J. H. Chong and M. J. MacLachlan, *Inorg. Chem.*, 2006, **45**, 1442.
55 N. G. White and M. J. MacLachlan, *J. Org. Chem.*, 2015, **80**, 8390.
56 S. Lehtola, C. Steigemann, M. J. T. Oliveira and M. A. L. Marques, *SoftwareX*, 2018, **7**, 1.
57 F. Neese, *Wiley Interdiscip. Rev.:Comput. Mol. Sci.*, 2022, **12**, e1606.
58 E. F. Valeev, *Libint*, 2.8.0 edn, 2022.
59 F. Weigend, *Phys. Chem. Chem. Phys.*, 2006, **8**, 1057.
60 F. Weigend and R. Ahlrichs, *Phys. Chem. Chem. Phys.*, 2005, **7**, 3297.
61 P. Biegger, S. Stolz, S. N. Intorp, Y. Zhang, J. U. Engelhart, F. Rominger, K. I. Hardcastle, U. Lemmer, X. Qian and M. Hamburger, *J. Org. Chem.*, 2015, **80**, 582.
62 M. Muller, H. Reiss, O. Tverskoy, F. Rominger, J. Freudenberg and U. H. F. Bunz, *Chem.–Eur. J.*, 2018, **24**, 12801.
63 R. Ushiroguchi, Y. Shuku, R. Suizu and K. Awaga, *Cryst. Growth Des.*, 2020, **20**, 7593.
64 K. Pagano, J. G. Kim, J. Luke, E. Tan, K. Stewart, I. V. Sazanovich, G. Karras, H. I. Gonev, A. V. Marsh, N. Y. Kim, S. Kwon, Y. Y. Kim, M. I. Alonso, B. Dörling, M. Campoy-Quiles, A. W. Parker, T. M. Clarke and Y.-H. Kim, *Nat. Commun.*, 2024, **15**, 6153.
65 S. Wood, J. R. Hollis and J.-S. Kim, *J. Phys. D: Appl. Phys.*, 2017, **50**, 073001.
66 T. M. Krygowski, *J. Chem. Inf. Comput. Sci.*, 1993, **33**, 70.
67 J. M. Marin-Beloqui, S. Gomez, H. I. Gonev, M. Comi and M. Al-Hashimi, *Chem. Sci.*, 2023, **14**, 812.
68 C. L. Hilton, C. R. Jamison, H. K. Zane and B. T. King, *J. Org. Chem.*, 2009, **74**, 405.
69 N. T. Tsui, A. J. Paraskos, L. Torun, T. M. Swager and E. L. Thomas, *Macromolecules*, 2006, **39**, 3350.
70 M. Kasha, H. R. Rawls and M. Ashraf El-Bayoumi, *Pure Appl. Chem.*, 1965, **11**, 371.
71 A. Kunz, N. Oberhof, F. Scherz, L. Martins, A. Dreuw and H. A. Wegner, *Chem.–Eur. J.*, 2022, **28**, e202200972.
72 M. J. Ahrens, L. E. Sinks, B. Rybtchinski, W. Liu, B. A. Jones, J. M. Giaimo, A. V. Gusev, A. J. Goshe and D. M. Tiede, *J. Am. Chem. Soc.*, 2004, **126**, 8284.
73 M. Hecht and F. Würthner, *Acc. Chem. Res.*, 2021, **54**, 642.
74 B. Rybtchinski, L. E. Sinks and M. R. Wasielewski, *J. Phys. Chem. A*, 2004, **108**, 7497.
75 F. Würthner, *Acc. Chem. Res.*, 2016, **49**, 868.
76 H. Langhals and W. Jona, *Angew. Chem., Int. Ed.*, 1998, **37**, 952.
77 Physical Constants of Organic Compounds, in *CRC Handbook of Chemistry and Physics*, ed. J. R. Rumble, CRC Press/Taylor & Francis, Boca Raton, FL, 106th edn, 2025.
78 C. Schafer, R. Ringstrom, J. Hanrieder, M. Rahm and B. Albinsson, *Nat. Commun.*, 2024, **15**, 8705.
79 A. Gilbert and J. Baggott, *Essentials of Molecular Photochemistry*, Blackwell Scientific Publications, 1991.
80 T. E. Kaiser, H. Wang, V. Stepanenko and F. Würthner, *Angew. Chem., Int. Ed.*, 2007, **46**, 5541.
81 T. E. Kaiser, V. Stepanenko and F. Würthner, *J. Am. Chem. Soc.*, 2009, **131**, 6719.
82 H. Piwonski, S. Nozue, H. Fujita, T. Michinobu and S. Habuchi, *Nano Lett.*, 2021, **21**, 2840.
83 U. Barotov, D. H. T. Arachchi, M. D. Klein, J. Zhang, T. Sverko and M. G. Bawendi, *Adv. Opt. Mater.*, 2023, **11**, 2201471.
84 T. Cardeynaels, S. Paredis, A. Danos and A. Harrison, *Dyes Pigm.*, 2021, **190**, 109301.
85 P. Gu, T. He, Z. Wang and S. Wang, *Chem. Sci.*, 2024, **15**, 13351.
86 C. A. Richard, Z. Pan, H. Y. Hsu and S. Cekli, *ACS Appl. Mater. Interfaces*, 2014, **6**, 5221.
87 Y. He, N. Okamoto, T. Maeda and H. Nakazumi, *J. Jpn. Soc. Colour Mater.*, 2017, **90**, 51.
88 C. A. Richard, Z. Pan, A. Parthasarathy and F. A. Arroyave, *J. Mater. Chem. A*, 2014, **2**, 9866.
89 J. B. Birks, *Photophysics of Aromatic Molecules*, Wiley-Interscience, 1970.
90 F. Würthner, T. E. Kaiser and C. R. Saha-Möller, *Angew. Chem., Int. Ed.*, 2011, **50**, 3376.
91 Q. Liu and K. Vandewal, *Adv. Mater.*, 2023, **35**, e2302452.
92 P. Bi, S. Zhang, Z. Chen and Y. Xu, *Joule*, 2021, **5**, 2408.
93 Z. E. Dance, S. M. Mickley and T. M. Wilson, *J. Phys. Chem. A*, 2008, **112**, 4194.
94 Y. Dong, A. A. Sukhanov and J. Zhao, *J. Phys. Chem. C*, 2019, **123**, 22793.
95 M. Hussain, A. M. El-Zohry and Y. Hou, *J. Phys. Chem. B*, 2021, **125**, 10813.
96 S. Medina Rivero, M. J. Alonso-Navarro, C. Tonnele and J. M. Marin-Beloqui, *J. Am. Chem. Soc.*, 2023, **145**, 27295.
97 K. M. Lefler, K. E. Brown and W. A. Salamant, *J. Phys. Chem. A*, 2013, **117**, 10333.
98 Y. Hirata and I. Tanaka, *Chem. Phys. Lett.*, 1976, **43**, 568.
99 M. A. El-Sayed, *J. Chem. Phys.*, 1963, **38**, 2834.
100 M. Baba, *J. Phys. Chem. A*, 2011, **115**, 9514.
101 K. Baumgärtner, M. Hofmann, F. Rominger, S. M. Elbert, A. Dreuw and M. Mastalerz, *J. Org. Chem.*, 2020, **85**, 15256.
102 G. Preda, R. Mobili, D. Ravelli, V. Amendola and D. Pasini, *J. Org. Chem.*, 2024, **89**, 5690.
103 P. Lei, S. Zhang, N. Zhang, X. Yin, N. Wang and P. Chen, *ACS Omega*, 2020, **5**, 28606.

104 T. Nakazawa and I. Murata, *J. Am. Chem. Soc.*, 1977, **99**, 1996.
105 I. Murata, *Pure Appl. Chem.*, 1983, **55**, 323.
106 Y. Zhang, D. Zhang and T. Huang, *Angew. Chem., Int. Ed.*, 2021, **60**, 20498.
107 H. C. Friedman, E. D. Cosco and T. L. Atallah, *Chem*, 2021, **7**, 3359.
108 Y.-C. Tsai, Y.-C. Chen and H.-F. Liu, *J. Am. Chem. Soc.*, 2025, **147**, 21940.
109 W. Lowrie, R. J. E. Westbrook and J. Guo, *J. Chem. Phys.*, 2023, **158**, 110901.
110 S. J. Coles, D. R. Allan and C. M. Beavers, *Structure and Bonding*, Springer, 2020, vol. 5, pp. 69–140.
111 (*a*) CCDC 2495341: Experimental Crystal Structure Determination, 2026, DOI: 10.5517/ccdc.csd.cc2prlwy; (*b*) CCDC 2502203: Experimental Crystal Structure Determination, 2026, DOI: 10.5517/ccdc.csd.cc2pzr7p.